Fatigue Characteristics of 7050-T7451 Aluminum Alloy Friction Stir Welding Joints and the Stress Ratio Effect

(Article begins on next page)

15 January 2025

Article

Fatigue Characteristics of 7050-T7451 Aluminum Alloy Friction Stir Welding Joints and the Stress Ratio Effect

Hanji Zhu, Giuseppe Lacidogna, Caiyan Deng, Baoming Gong and Fei Liu

Topic

Recent Advances in Structural Health Monitoring

Edited by
Prof. Dr. Giuseppe Lacidogna, Prof. Dr. Sanichiro Yoshida, Prof. Dr. Guang-Liang Feng,
Prof. Dr. Jie Xu, Dr. Alessandro Grazzini and Dr. Gianfranco Piana

Article

Fatigue Characteristics of 7050-T7451 Aluminum Alloy Friction Stir Welding Joints and the Stress Ratio Effect

Hanji Zhu [1], Giuseppe Lacidogna [2], Caiyan Deng [1,*], Baoming Gong [1] and Fei Liu [3]

1 Key Laboratory of Advanced Joining Technology of Tianjin, Department of Materials Science and Engineering, Tianjin University, Road Weijin 92, Tianjin 300072, China
2 Department of Structural, Geotechnical and Building Engineering, Politecnico di Torino, Corso Duca degli Abruzzi 24, 10129 Torino, Italy
3 China Jingye Engineering Technology Co., Ltd., Xitucheng Road 33, Beijing 100088, China
* Correspondence: dengcy@tju.edu.cn; Tel.: +86-22-85356663

Abstract: The fatigue crack initiation and growth characteristics in 7050-T7451 aluminum alloy butt joints subjected to different stress ratios and owing to friction stir welding (FSW) were investigated using fatigue tests for stress ratios of 0.1, 0.3, and 0.5. The difference between the fatigue crack initiation in the base material (BM) and FSW joints, related to coarse secondary phases, was explored using scanning electron microscopy (SEM). Accordingly, $Al_{23}CuFe_4$, Al_7Cu_2Fe, and $Al_2Mg_3Zn_3$ were the preferred joint crack initiation locations, whereas Mg_2Si was the major fracture initiation point of the parent material, and cracks tended to propagate along dense, coarse secondary phases, becoming more pronounced for larger cracks. In addition, as the stress ratio increased, non-Mg_2Si phase fracture initiation points appeared in the BM. Meanwhile, the quantity of non-Mg_2Si phases in the joints continued to increase, and the crack initiation sites became increasingly concentrated in the TMAZ-HAZ region.

Keywords: fatigue; 7050-T7451 aluminum alloy; FSW; stress ratio; coarse inclusion phase

1. Introduction

High-strength aluminum alloys have been widely used in the aerospace industry and high-speed vehicles owing to their low density and high strength-to-weight ratio [1]. However, owing to their high thermal conductivity and strong oxidation susceptibility, $7\times\times\times$ aluminum alloys have been difficult to be jointed using conventional fusion-welding techniques. These issues were resolved using the friction stir welding (FSW) technology, which has led to the widespread use of poorly welded high-strength aluminum alloys [2–4]. Therefore, the fatigue performance of high-strength aluminum alloys and their welded joints is a crucial factor affecting the safety and reliability of structures subjected to asymmetric alternating loads during their service time [5,6].

Recent studies have shown that coarse secondary phases play an important role in the fatigue behavior of aluminum alloys. Zheng et al. [7] investigated the effects of secondary-phase particles on the fatigue behavior of 2524-T34 aluminum alloy sheets and discovered that fatigue cracks primarily occurred at these secondary-phase particles and secondary-phase particle/substrate contact interfaces. According to Payne et al. [8], secondary phases are almost exclusively responsible for fatigue cracking, with most fatigue cracks starting at the loci of iron-rich secondary phases. Harlow et al. [9] found that only 3.5% of iron-rich secondary-phase cracks were subjected to cyclic loading, whereas approximately 87% of iron-rich secondary phases were observed in high-stress zones. Using nanoindentation techniques, Sudhanshu et al. [10] quantitatively and qualitatively evaluated secondary phases and discovered that the elastic moduli of iron-rich secondary phases were in the 130–169 GPa range, while those of Si-containing secondary phases were in the 44–97 GPa range. Using a four-point bending test on the AA7075-T651 alloy, Jin et al. [11] discovered

that the pre-cracked iron-rich secondary phase was responsible for the initiation of fatigue cracks. Another popular subject in fatigue research is the effect of mean stress. Deng et al. [12] performed ultrasonic fatigue tests on the 7050-T7451 aluminum alloy's FSW joints at R = −1, −0.3, and 0.3 and discovered that cracks primarily originated at the surface for higher mean stress levels, whereas for lower mean stress values, cracks were competitively nucleated in superficial and internal regions. Ma et al. [13] investigated the stress ratio effects on the fatigue-crack growth characteristics of 5083 aluminum alloys, and reported that the fatigue-crack propagation rate increased with increasing stress ratio, whereas the propagation threshold and fracture toughness decreased. Moreover, the average stress relaxation phenomenon was observed in the base material (BM) and weld regions as cyclic deformation proceeded. This phenomenon was more pronounced in the early stages of fatigue and weakened with increasing propagation, according to a thorough and in-depth study on the cyclic deformation of Ti-6Al-4V and Ti17 BMs and joints [14]. Jata et al. [15] studied the effect of the microstructure on the fatigue properties of the 7050-T7451 aluminum alloy's FSW joints and reported that the crack propagation rate in the stir zone (SZ) decreased at R = 0.33, while that in the heat-affected zone (HAZ) increased. At R = 0.7, the difference between the crack propagation rates for different zones was significantly smaller, owing to the intergranular damage mechanism in the SZ and residual stress in the HAZ. Moreover, the failure location in the studied FSW joints correlated well with the microstructure heterogeneity. Besel et al. [16] discovered that the SZ and the thermal–mechanical affected zone (TMAZ) of the 5024 aluminum alloy's FSW joint line tended to failure. The fatigue performance of the 6N01 aluminum alloy's FSW joints was studied by Sillapasa et al. [17], who reported that fatigue-related failures correlated with the hardness distribution in different joint regions and were more likely to occur in the HAZ with the lowest hardness. The strength gradient in the weld caused the plastic to concentrate in the HAZ, according to White et al. [18], who studied the impact of pre-stretching on the fatigue fracture initiation and mechanical behavior of the AA7050 aluminum alloy's FSW joints. However, the role of the coarse secondary phase has not yet been fully determined. The relationship between the fatigue behavior and coarse secondary-phase particles in FSW joints remains elusive.

As demonstrated above, while there have been numerous studies on secondary phases of aluminum alloys, the mechanism of crack initiation and the effect of the stress ratio of the different secondary phases in the base material and joints are not well studied in a systematic manner.

In this study, high-cycle fatigue tests were conducted on the aluminum alloy 7050-T7451 and its FSW joints, subjected to the stress ratios of 0.1, 0.3, and 0.5. The relationship between the coarse secondary phases and the preferred crack-initiation sites is discussed, and the irregular distribution of crack-initiation locations in joints subjected to various stress ratios is investigated.

2. Materials and Methods

2.1. Materials and FSW Joints

The BM was a rolled plate of the aluminum alloy 7050-T7451 with the dimensions of 12 mm × 1500 mm × 3000 mm. The chemical compositions and mechanical properties are listed in Tables 1 and 2, respectively. The rolled plate was divided into two flat plates with the dimensions of 700 mm × 70 mm × 12 mm, and the welding procedure was carried out using an HT-JM16 gantry FSW machine supplied by Aerospace Engineering Equipment (Suzhou, China) Co., Ltd. The stirring head was a threaded cone, and an I-shaped groove was adopted, with the welding direction parallel to the rolling direction of the plate. The specific welding process parameters are listed in Table 3 [19], while the friction-stir processing is shown schematically in Figure 1.

Table 1. Chemical composition of the 7050-T7451 aluminum alloy.

Zn	Mg	Cu	Fe	Si	Mn	Ti	Al
5.89	2.59	1.98	0.29	0.10	0.10	0.05	Remaining

Table 2. Mechanical properties of the 7050-T7451 aluminum alloy.

R_{eL}/MPa	R_m/MPa	A (%)	HV
492	560	12	150

Table 3. FSW parameters.

Spinning Speed /r·min^{-1}	Welding Speed /mm·min^{-1}	Inclination /°	Depression /mm
300	80	2.5	0.1
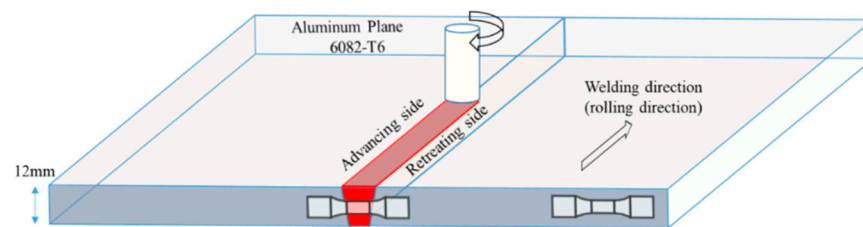
Figure 1. Schematic of the friction-stir processing.

2.2. Hardness Test and Characteristic Areas

A hardness test across the entire weld joint was conducted on the middle line of the thickness, using an HV-1000A microhardness tester (made in Shanghai, China). The hardness test utilized an indent spacing of 0.15 mm for the TMAZ and SZ and 0.2 mm for the BM and HAZ, a load of 3 kgf, and a loading and holding time of 15 s. The specimens used for the hardness test were ground using a wet sandpaper to 7000 mesh before being polished with a diamond sus-pension (particle size, 0.25 μm) to remove the influence of the surface-hardening layer. Figure 2a shows the W-shaped hardness distribution for the FSW joints. Accordingly, an FSW joint could be divided into four areas: (1) BM, (2) HAZ, (3) TMAZ, and (4) SZ. The advancing side was the tangential direction of the stirring needle rotation, while the other side was the retreating side (RS), as shown in Figure 2b.

(a)

Figure 2. *Cont.*

(**b**)
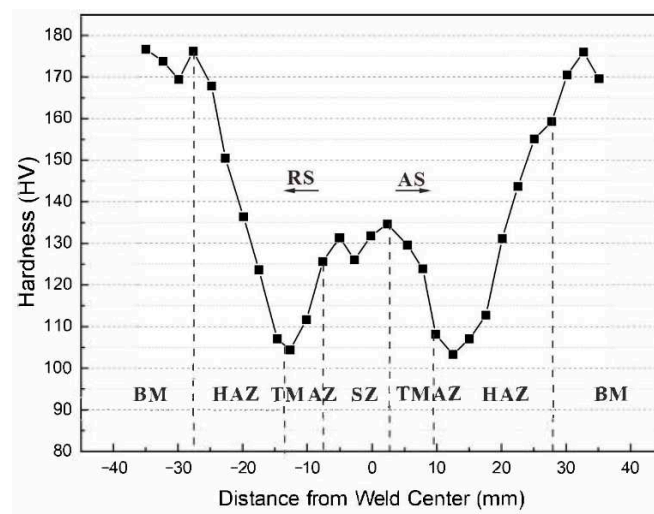
Figure 2. Results of the hardness test: (**a**) hardness distribution in FSW joints and (**b**) macroscopic morphology of aluminum alloy FSW joints.

2.3. Fatigue Test

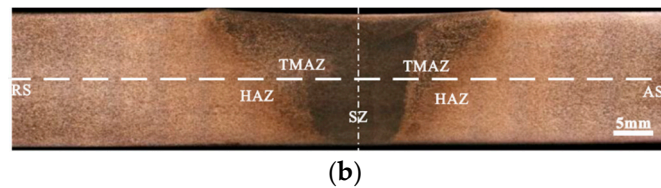Fatigue tests on specimens subjected to different stress ratios were conducted using a GPS200 high-frequency fatigue test machine in an ambient environment. The specimens of the 7075-T7451 aluminum alloy BM and FSW butt joints in Figure 3 were tested until failure at the three stress ratios of R = 0.1, 0.3, and 0.5 at the frequency of approximately 100 Hz. The specimen mark was in the 'type/stress/ratio number' format. For instance, serial number M-1-1 designated the first fatigue specimen of the BM with the stress ratio of 0.1, while J-3-3 designated the third fatigue specimen of the FSW joint with the stress ratio of 0.3.
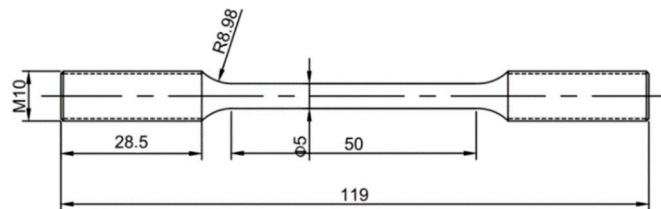
Figure 3. Specimen dimensions for fatigue studies.

A comparison of the fatigue S–N curves for various stress ratios of the BM and joints is shown in Figure 4. At 10^7 cycles, the fatigue strengths for the BM were 254, 228, and 175 MPa, respectively, whereas for the FSW joints, the conditional fatigue strengths were 193, 177, and 138 MPa, respectively. In addition, the fatigue strengths of the FSW joints were approximately 20% lower than those of the BMs subjected to the same stress ratios; in all the cases, the fatigue strengths decreased as the stress ratio increased. Test results are given in Appendix A.
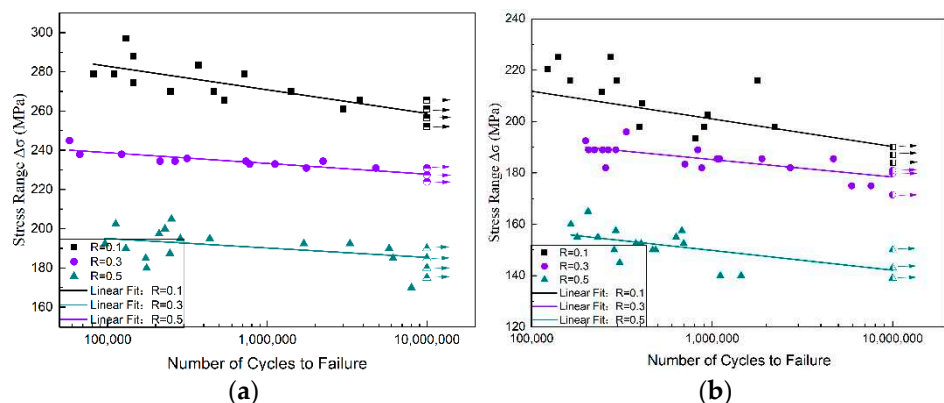
Figure 4. Fatigue S–N curves of the BM and FSW joints: (**a**) fatigue S–N curves of the BM subjected to R = 0.1, 0.3, and 0.5; (**b**) fatigue S–N curves of the FSW joints subjected to R = 0.1, 0.3, and 0.5.

2.4. Metallography Preparation and Analysis

The specimens for the optical microscopy (OM) analysis were cut perpendicular to the welding direction and prepared following the metallography procedures described in Section 2.2. Keller's reagent was used for the etching after polishing. Metallographic

observations were performed using an OLYMPUS-GX51 microscope (Shinjuku, Japan). The fracture surface was observed using a JSM-7800F scanning electron microscope (SEM, JEOL, Akishima, Japan) equipped with an energy spectrometer and a backscatter probe. By selecting appropriate gray threshold values, secondary phases were identified and analyzed using the Image-Pro Plus 6.0 software.

3. Results

3.1. Microstructure Observations

3.1.1. Metallographic Analysis

The welding process can have a significant impact on the microstructure, and large angular grain boundaries are dangerous locations for fatigue failure of the specimen [20]. The microstructures of the characteristic regions of the FSW joints are shown in Figure 5. Fine and uniformly distributed equiaxial grains were generated during the fully recrystallized process in the SZ, owing to the severe deformation and sufficient frictional heat, as shown in Figure 5a. The TMAZ between the HAZ and SZ was characterized by a highly deformed structure, whereas the lower thermal input in this zone did not provide sufficient driving force for dynamic recrystallization. Because the HAZ was unaffected by stirring, the grain structure was virtually identical to that of the BM, as shown in Figure 5b. The black particles in Figure 5 are the coarse secondary phases in the matrix, which exhibit different morphologies owing to the thermal–mechanical variation of the welding process. In contrast to the TMAZ, where only a slightly coarse secondary phase was observed owing to the lower temperature, the secondary-phase size in the SZ was much finer after directly contacting the stirring pin, as shown in Figure 5c. The same coarsening phenomenon took place in the HAZ, although the comparison between Figure 5d,e indicates that the size of the coarse secondary phase in the HAZ was larger than that in the SZ. As shown in Figure 5f, the BM contained two different types of coarse secondary-phase particles, that is, white and gray–black particles, as reported by SEM.

Figure 5. *Cont.*

(e)

(f)
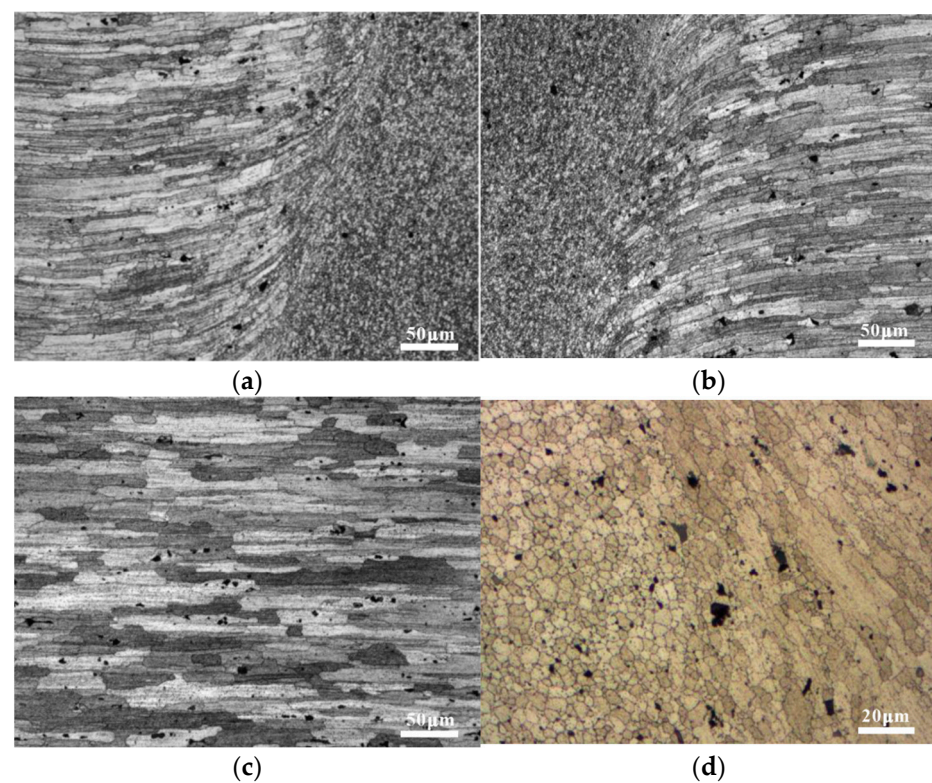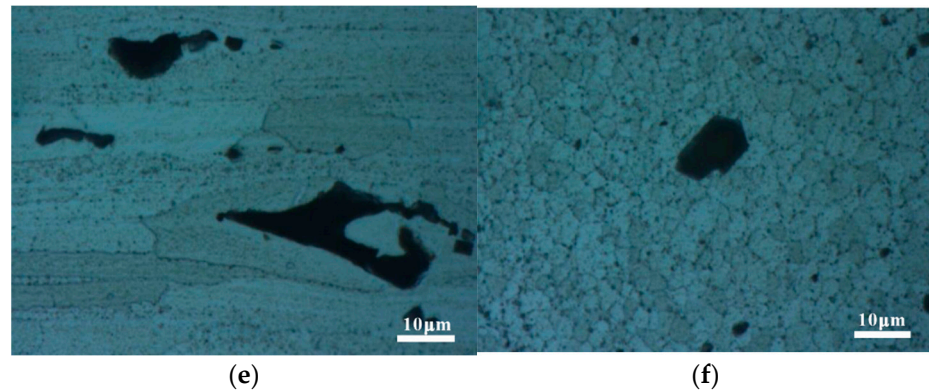
Figure 5. Microstructure of the 7050 aluminum alloy's FSW joints: (**a**) the TMAZ-SZ; (**b**) the HAZ; (**c**) high-magnification morphology of the TMAZ-SZ; (**d**) secondary-phase morphology of the HAZ; (**e**) secondary-phase morphology of the SZ; (**f**) SEM of the BM.

3.1.2. Coarse Secondary Phases

The coarse secondary phases were characterized via selected-area diffraction by TEM analysis, and the results are shown in Figure 6. The gray–black coarse secondary phase in Figure 5f is Mg_2Si, while the white coarse secondary phases mainly consist of $Al_{23}CuFe_4$, Al_7Cu_2Fe, and $Al_2Mg_3Zn_3$, based on the atomic number calibration analysis. In the BM, only the Mg_2Si phase appears to be gray–black, while all the other non-Mg_2Si phases are white. The coarse secondary phase in the BM is categorized into Mg_2Si and non-Mg_2Si phases, in agreement with the gray difference of the coarse secondary phase under the backscatter lens, to enable further statistical analysis.

(a)

(b)

(c)

(d)
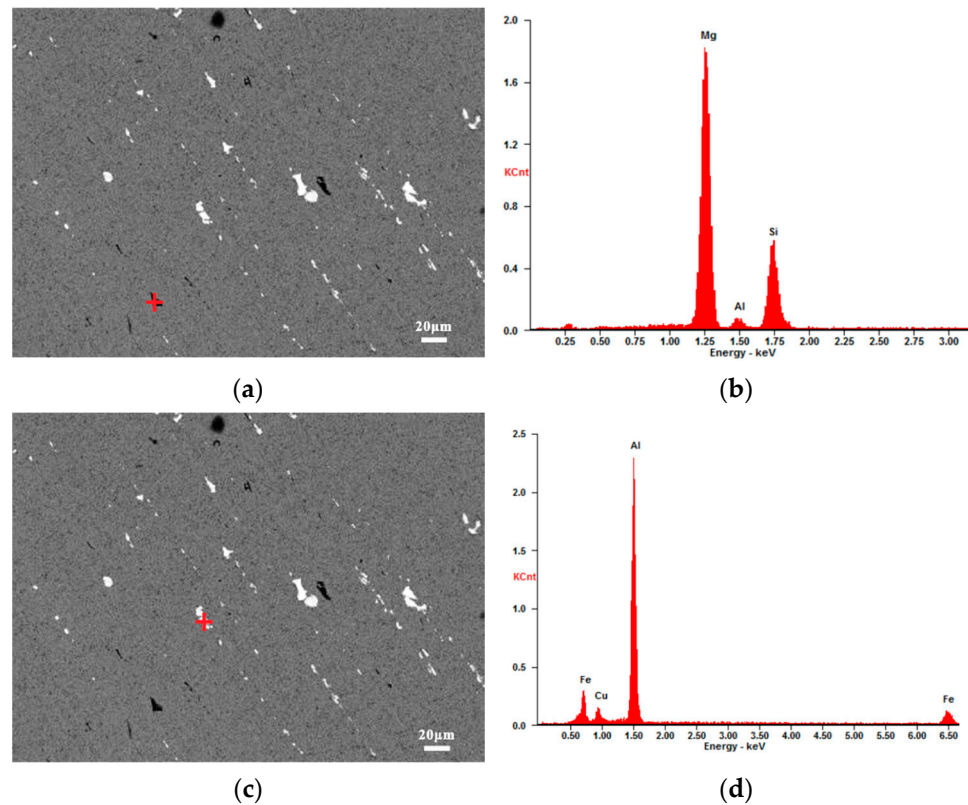
Figure 6. *Cont.*
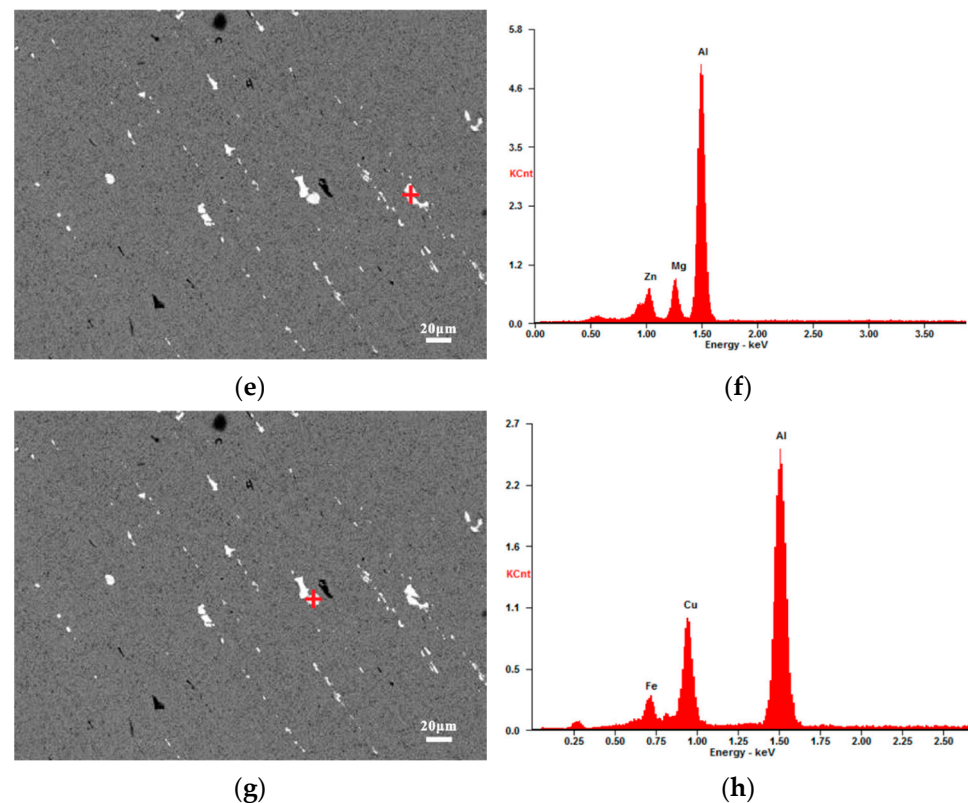
Figure 6. EDS spectra of the secondary phases: (**a,c,e,g**) SEM images of the matrix; (**b**) Mg_2Si; (**d**) $Al_{23}CuFe_4$; (**f**) $Al_2Mg_3Zn_3$; (**h**) Al_7Cu_2Fe.

3.2. Fatigue Crack-Initiation Mechanism

The mechanism of the fatigue crack emergence in the high-circumference range was the primary focus of this study. Because fatigue crack initiation and early growth account for most of the fatigue life, the impact of the FSW on the microstructure complicates the fatigue crack-initiation mechanism. Fine precipitates are common sites for fatigue crack nucleation in aluminum alloys. The constituent particle's size and shape are important characteristics that influence crack nucleation. Additionally, differences in stiffness and thermal expansion coefficients between the inclusion and the surrounding matrix can introduce a localized stress concentration in and around a particle which increases the likelihood of fatigue crack formation. Fatigue cracks often form at inclusions by one of three mechanisms: inclusion cracking, debonding of the interface between the inclusion and matrix, or cracking at lines of slip in the surrounding matrix [21]. According to experimental observations, two distinct crack-nucleation mechanisms can be identified: (i) cracks nucleate in the bulk of the coarse secondary phase, and (ii) cracks emerge at the interface between the secondary phase and the matrix. It is widely thought that the former mechanism dominates crack nucleation in the case of non-Mg_2Si phases, while both mechanisms coexist in the case of Mg_2Si secondary phases.

Figure 7a,b show that the initiation, stable propagation, and final fracture regions can be identified. Furthermore, as shown in Figure 7c,d, some coarse secondary phases on the surfaces of the BM and FSW joint specimens could be identified as sole crack-initiation sites. According to the studies of energy spectra, the coarse secondary phases at the crack initiation sites were Mg_2Si for the BM and $Al_{23}CuFe_4$ for the joints (see Appendix B for the morphology description). Moreover, the statistical results of the fatigue fractures in Figure 8 demonstrated that 78 of 97 fatigue fractures in the BM and joints were coarse secondary-phase-initiated cracks, while 32 of 38 of the BM specimens were cracked by the coarse secondary-phase Mg_2Si, whereas the non-Mg_2Si phase ($Al_2Mg_3Zn_3$, $Al_{23}CuFe_4$, and Al_7Cu_2Fe) cracking accounted for 32 of the 40 fractures in the joint specimens. The

gray–black Mg_2Si phase was the primary cracking phase for the BM specimens, whereas the white secondary phase was the primary cracking site for the joint specimens. Therefore, secondary phases are the predominant fatigue crack-initiation sites in the 7050-T7451 aluminum alloy, regardless of the BM and FSW joints.
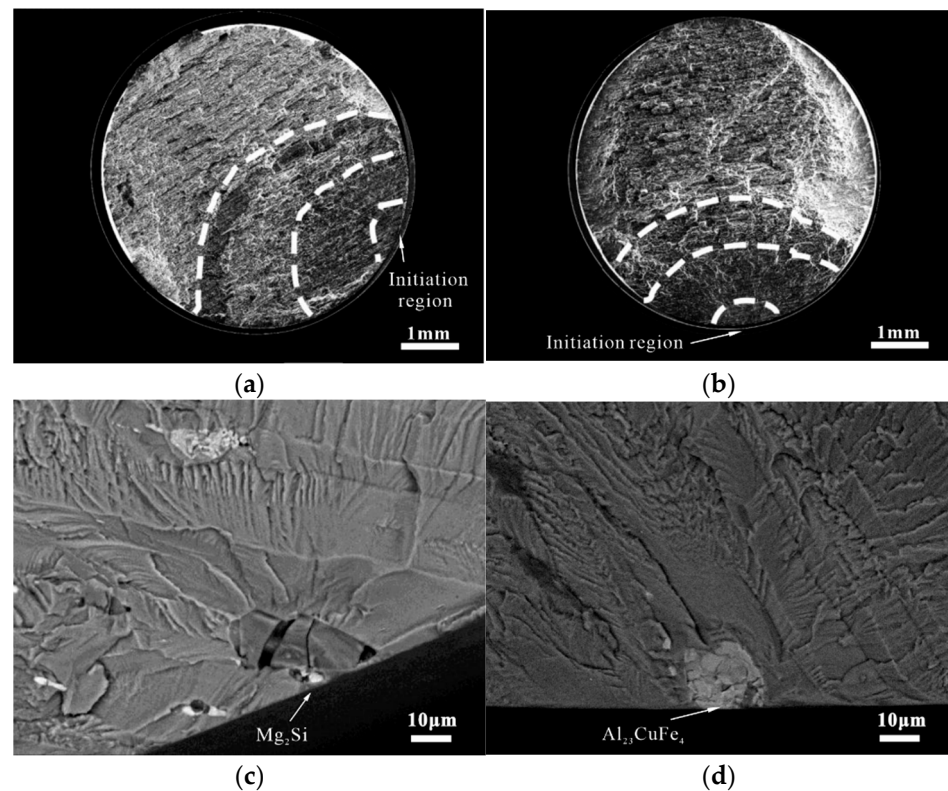
Figure 7. Fatigue fracture morphology: (**a**) M-3-1# sample macroscopic fracture; (**b**) J-3-23# sample macroscopic fracture; (**c**) M-3-1# sample origin morphology; (**d**) J-3-23# sample origin morphology.
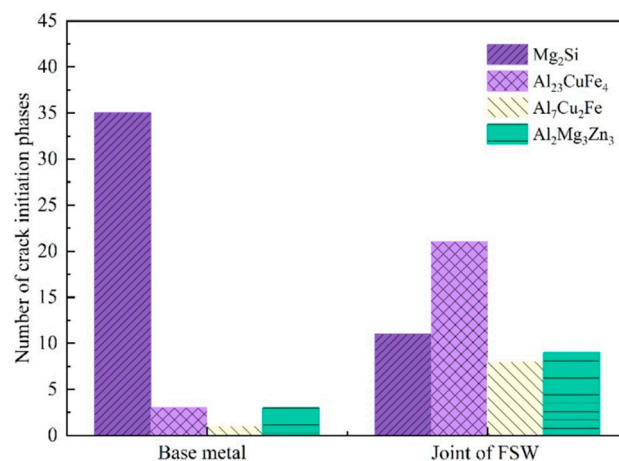
Figure 8. Initiation phase statistics for the BM and FSW joints.

The major cracking phase of the BM specimens was Mg_2Si, which was the only stable intermetallic phase in the Mg-Si binary alloy. Although the Mg_2Si phase has excellent mechanical properties, it is highly brittle and has low ductility, as shown in Figure 9 [22]. The backscattered electron images in Figure 10 illustrate the status of the coarse secondary-phase Mg_2Si on the fracture surface, which is fragmented and debonded from the matrix. Figure 10b shows the small craters owing to the Mg_2Si debonding from the substrate and the serrated cracks at the edges, which indicates that cracks tended to initiate in the

bulk Mg_2Si, with the subsequent coalescence and deflection of microcracks along the interface leading to serrated cracks. Although the Si content in the 7050 aluminum alloy was only 0.10%, its size was similar to that of Al_2CuMg, and most of the Mg_2Si phase observed at the broad transverse side was internally broken. However, the non-Mg_2Si phase was tightly bound to the matrix, as shown in Figure 9b, causing an interfacial stress concentration or singularity owing to the elastic deformation inconsistency. This type of crack nucleation exhibited distinct fatigue cracks and extension marks on the bond surface on the microscopic level, as shown in Figure 11.

(a) **(b)**
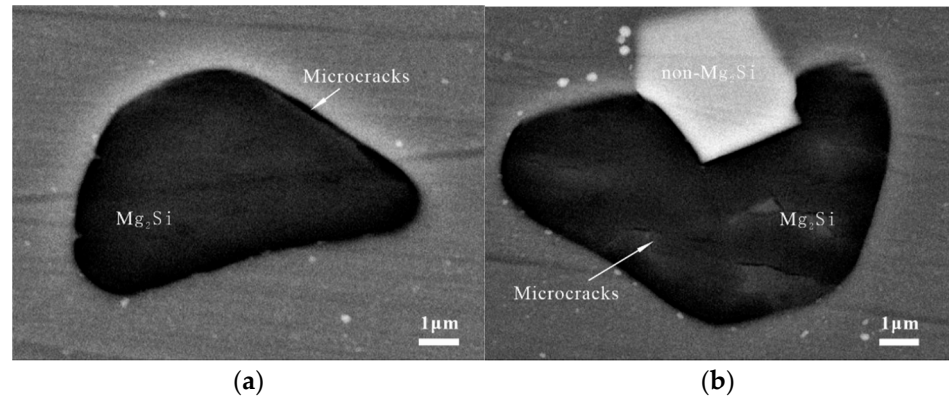
Figure 9. Coarse secondary phase in the initial state of the BM: (**a**) microcracks in the BM of the Mg_2Si phase; (**b**) Mg_2Si phase with internal microcracks and various non-Mg_2Si phases.

(a) **(b)**
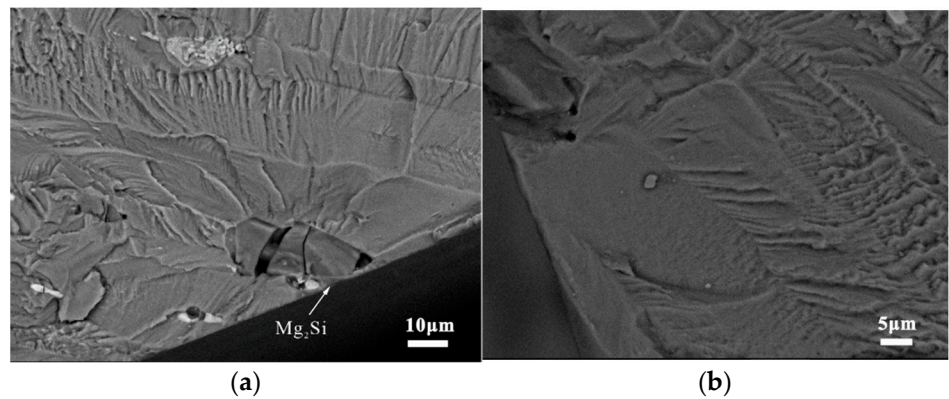
Figure 10. Mg_2Si phase cracking at the BM specimens' fracture: (**a**) Mg_2Si phase internal fracture; (**b**) Mg_2Si phase debonding, with serrated cracks near the edge.

(a) **(b)**
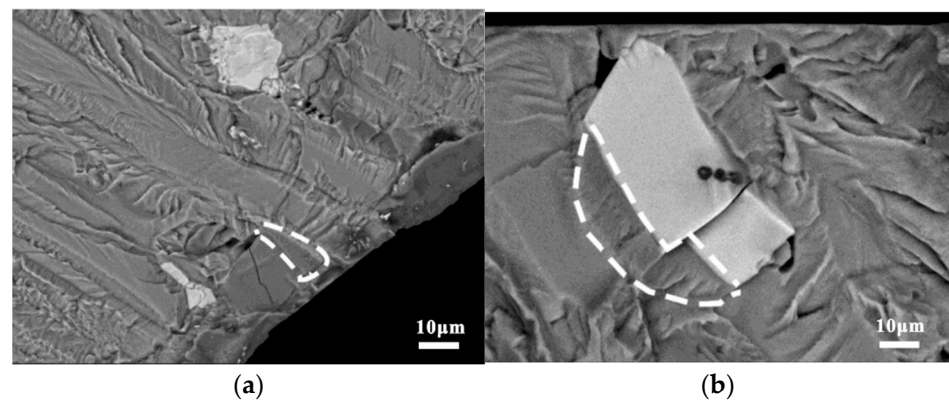
Figure 11. Interfacial type cracking in the BM specimens: (**a**) Mg_2Si phase and (**b**) non-Mg_2Si phase.

Figure 12a,b show the craters generated following the debonding of the Mg$_2$Si phase, which indicates that the crack initiation mechanism of the Mg$_2$Si phase in the joints was the same as in the BM. The thermomechanical deformation of FSW might have worsened the bonding strength between the Mg$_2$Si phase and the matrix. Figure 13a shows the internal cracking of the large non-Mg$_2$Si phase (50 μm), which was first subjected to external forces. Subsequently, the cracks gradually spread across the interface into the matrix as a result of the cyclic loading. As shown in Figure 13b, the crack growth in the non-Mg$_2$Si phase can be divided into two distinct regions: (1) a smooth region created by instantaneous fracture close to the specimen surface and (2) a rough region with signs of stable crack extension far away from the specimen surface.

(**a**)　　　　　　　　　　　　　　　　　　　　　(**b**)
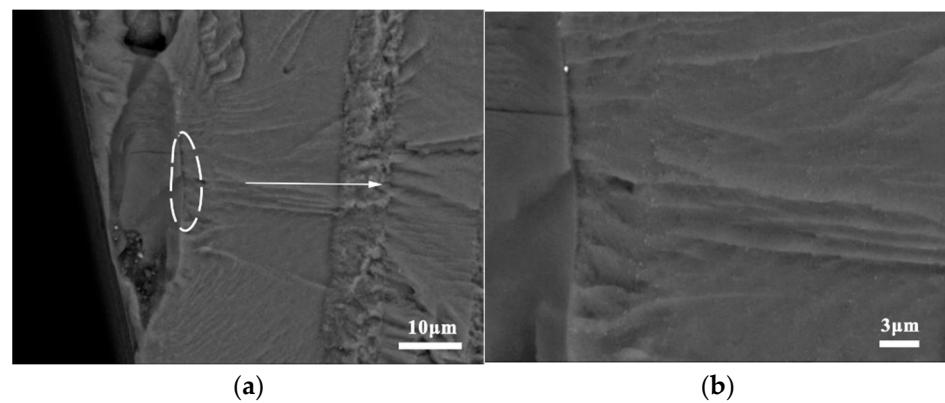
Figure 12. Cracking of the Mg$_2$Si phase in joint specimens: (**a**) debonding of the Mg$_2$Si phase and (**b**) serrated cracks.

(**a**)　　　　　　　　　　　　　　　　　　　　　(**b**)
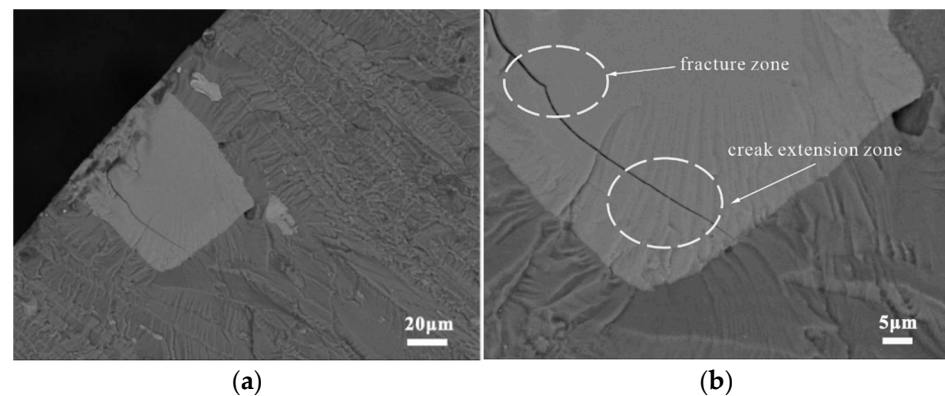
Figure 13. Cracking of the non-Mg$_2$Si phase in joint specimens: (**a**) origin of the fracture pattern and (**b**) local magnification.

The distribution of the coarse secondary phase on the fracture surface, for various phases of the fatigue crack extension, was investigated for determining the impact of the coarse secondary phase on the fatigue crack extension. The results are shown in Figure 14. The Image Pro J 6.0 software was used for determining the geometrical parameters of the secondary phases. The processing results are shown in Figure 14d–f,j–l. According to the distribution of the coarse secondary phase on the fracture surface, the density of the phase gradually increased as the crack propagated. When the crack propagates in the full joint specimen, it is more likely to propagate along the direction where the strength of the entire joint is the lowest and the coarse secondary phase is the most densely distributed. This is also confirmed in the article by Liu [23]. This provided credible experimental results for future research.
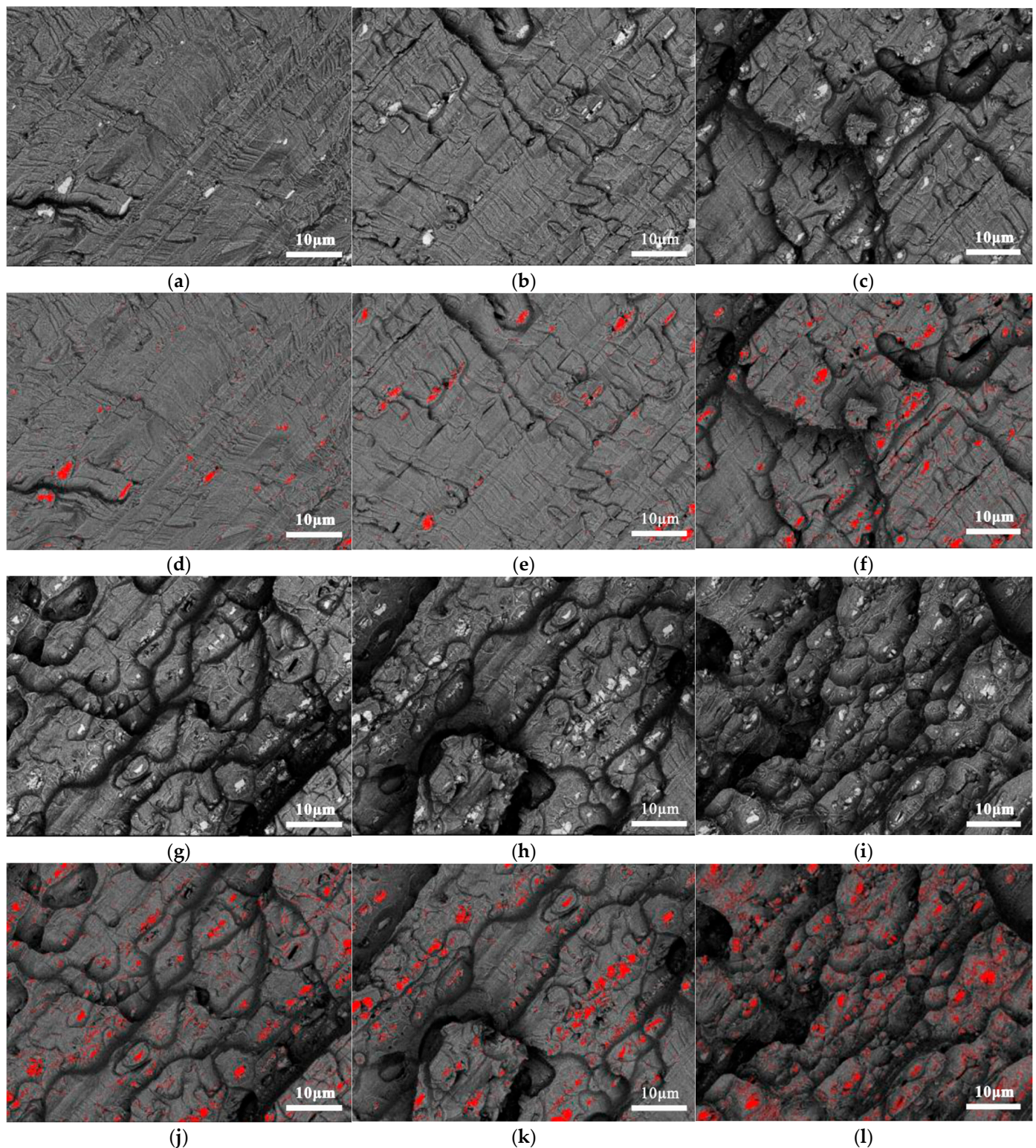
Figure 14. Distribution of the coarse secondary phase, during different stages of the fatigue crack extension: (**a**) early expansion stage; (**b**) stable expansion stage; (**c**) boundary between the stable and unstable expansion stages; (**g**) unstable expansion stage I; (**h**) unstable expansion stage II; (**i**) unstable expansion stage III. (**d**) processed image, (**e**) processed image, (**f**) processed image, (**j**) processed image, (**k**) processed image, (**l**) processed image.

3.3. Effect of the Stress Ratio on the Fatigue Behavior

The numbers of the cracking phases in the joint and BM specimens for the Mg_2Si and non-Mg_2Si phases for the three stress ratios are listed in Table 4. For the BM specimens, the primary cracking phase was Mg_2Si. However, as the stress ratio increased, non-Mg_2Si phase cracks appeared. For the joint specimens, most of the cracked phase was the non-Mg_2Si phase at low mean stress values, and this phenomenon became more pronounced as the stress ratio increased. In the BM, the stress concentration at the non-Mg_2Si and matrix interface was insufficient to cause crack initiation when the stress was relatively low. For the FSW joints, the specimens were primarily broken in the non-Mg_2Si phase, and internal cracking was more likely to extend to the matrix. This behavior became more obvious at higher stress ratios. Figure 15 summarizes the average areas of the crack initiation-related secondary phases for the different specimens subjected to the different considered stress ratios. At the stress ratios of 0.1, 0.3, and 0.5, the average areas of the cracked phases for the BM specimens were 514 μm^2, 432 μm^2, and 378 μm^2, and the average areas of the cracked phases for the joint specimens were 323 μm^2, 293 μm^2, and 288 μm^2, respectively. The cracking phase areas for the BMs were greater than for the joint specimens and decreased noticeably as the stress ratio increased.

Table 4. Summary statistics for different secondary phases.

Crack Initiation Phase	BM Specimen			FSW Specimen		
	R = 0.1	R = 0.3	R = 0.5	R = 0.1	R = 0.3	R = 0.5
Mg_2Si	13	12	10	5	5	1
$Al_{23}CuFe_4$	0	0	3	6	6	9
Al_7Cu_2Fe	0	1	0	3	3	2
$Al_2Mg_3Zn_3$	0	1	2	3	2	4
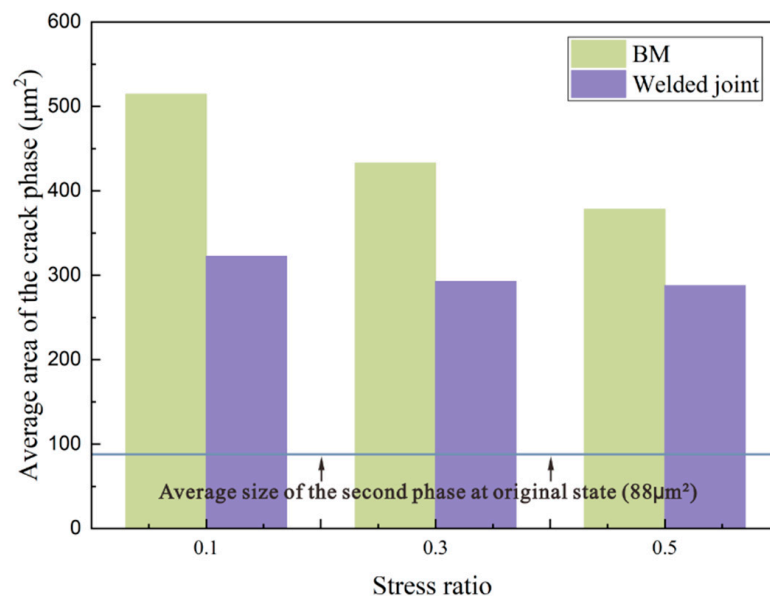
Figure 15. Average area of cracked phase for different stress ratios.

3.4. Effect of the Stress Ratio on the Fracture Location in Joint Specimens

The fracture-location statistical analysis was performed for all specimens, and only the results for the FSW specimens are plotted in Figure 16 for clarity. It was found that the fracture locations in the BM specimens were randomly distributed along the gauge; in contrast, only a few FSW specimens were fractured at the SZ or HAZ, whereas most failures occurred preferentially in the TMAZ-HAZ. It was also found that as the stress ratio increased from R = 0.1 to R = 0.5, the crack initiation sites tended to aggregate in the TMAZ and HAZ regions.
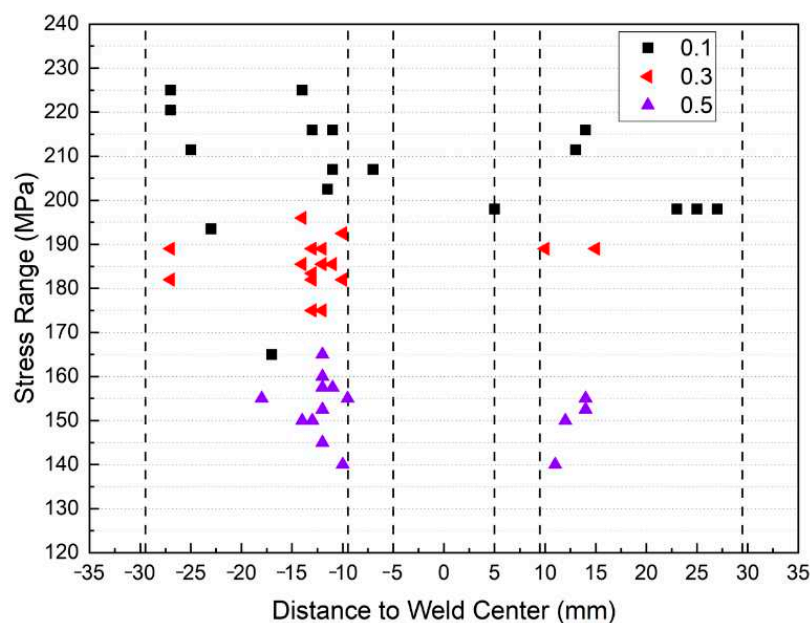
Figure 16. Characterization of the FSW joint fracture locations for different stress ratios.

4. Conclusions

This study determined that coarse secondary phases served as the main fatigue crack-initiation sites for the BM and FSW joints of the 7050-T7451 aluminum alloy. Fractographic analyses demonstrated that $Al_{23}CuFe_4$, Al_7Cu2Fe, and $Al_2Mg_3Zn_3$ were the preferred joint crack-initiation sites, whereas Mg_2Si was the major fracture-initiation point of the parent material. Two distinct crack-nucleation mechanisms were identified: (1) crack nucleation in the bulk of the non-Mg_2Si phases such as $Al_{23}CuFe_4$, Al_7Cu_2Fe, and $Al_2Mg_3Zn_3$ and (2) crack initiation at the Mg_2Si–matrix interface. The former mechanism accounted for 77.6% of the FSW joint specimens, whereas 83.3% of the cracks formed in the BM specimens owing to the latter mechanism. In addition, as the stress ratio increased, non-Mg_2Si phase fracture initiation points appeared in the BM. Meanwhile, the number of non-Mg_2Si phases in the joints continued to increase, and the crack initiation sites became increasingly concentrated in the TMAZ-HAZ region.

Appendix A

Table A1. Fatigue results of 7050 aluminum alloy base metal.

Specimen	σ_a (MPa)	σ_{max} (MPa)	Fatigue Life (Cycles)	Result	Fracture Phase
M-1-1	279	310	81,661	fracture	Mg_2Si
M-1-2	270	300	248,588	fracture	Mg_2Si
M-1-3	261	290	1.00×10^7	run-out	-
M-1-4	265.5	295	3,802,212	fracture	Mg_2Si
M-1-5	265.5	295	537,795	fracture	Mg_2Si
M-1-6	261	290	1.00×10^7	run-out	-
M-1-7	261	290	1,848,259	fracture	Mg_2Si
M-1-8	261	290	2,991,520	fracture	Al-Zn-Mg-Cr
M-1-9	256.5	285	1.00×10^7	run-out	-
M-1-10	252	280	1.00×10^7	run-out	-
M-1-11	265.5	295	1.00×10^7	run-out	-
M-1-12	283.5	315	369,837	fracture	Mg_2Si
M-1-13	279	310	721,061	fracture	Mg_2Si
M-1-14	279	310	109,807	fracture	Mg_2Si
M-1-15	270	300	463,907	fracture	Mg_2Si
M-1-16	274.5	305	145,084	fracture	Mg_2Si
M-1-17	270	300	1,409,672	fracture	Mg_2Si
M-1-18	297	330	130,704	fracture	Mg_2Si
M-1-19	288	320	145,273	fracture	Mg_2Si
M-3-1	231	330	88,763	fracture	Mg_2Si
M-3-2	112	224	1.00×10^7	run-out	-
M-3-3	115.5	231	1,756,799	fracture	Mg_2Si
M-3-4	115.5	231	1.00×10^7	run-out	-
M-3-5	122.5	245	57,674	fracture	Mg_2Si
M-3-6	119	238	66,955	fracture	Mg_2Si
M-3-7	119	238	122,346	fracture	Mg_2Si
M-3-8	117.25	234.5	2,234,893	fracture	-
M-3-9	115.5	231	4,782,308	fracture	Mg_2Si
M-3-10	117.95	235.9	314,380	fracture	Mg_2Si
M-3-11	113.75	227.5	1.00×10^7	run-out	-
M-3-12	117.25	234.5	213,222	fracture	Al-Zn-Mg-Cr
M-3-13	117.25	234.5	264,515	fracture	Al_7Cu_2Fe+Al-Fe-Si
M-3-14	116.55	233.1	1,117,538	fracture	Mg_2Si
M-3-15	116.55	233.1	774,904	fracture	Mg_2Si
M-3-16	117.25	234.5	735,718	fracture	Mg_2Si
M-3-17	119	238	2,172,459	fracture	Mg_2Si
M-3-18	126	252	151,447	fracture	Mg_2Si
M-3-19	120.75	241.5	407,688	fracture	Mg_2Si
M-5-1	155	310	1.00×10^7	run-out	-
M-5-2	160	320	1.00×10^7	run-out	-
M-5-3	170	340	8,000,998	fracture	$Al_{23}CuFe_4$
M-5-4	175	350	1.00×10^7	run-out	-
M-5-5	180	360	175,588	fracture	Mg_2Si
M-5-6	165	330	1.00×10^7	run-out	-
M-5-7	170	340	1.00×10^7	run-out	-
M-5-8	190	380	5,801,306	fracture	Mg_2Si
M-5-9	192.5	385	96,353	fracture	Mg_2Si
M-5-10	195	390	436,398	fracture	Mg_2Si
M-5-11	192.5	385	1,694,327	fracture	Al-Zn-Mg-Cr
M-5-12	190	380	129,967	fracture	Al-Zn-Mg-Cr
M-5-13	187.5	375	245,626	fracture	Mg_2Si
M-5-14	180	360	1.00×10^7	run-out	-

Table A1. *Cont.*

Specimen	σ_a (MPa)	σ_{max} (MPa)	Fatigue Life (Cycles)	Result	Fracture Phase
M-5-15	185	370	173,310	fracture	$Al_{23}CuFe_4$
M-5-16	185	370	6,137,276	fracture	Al-Zn-Mg-Cr
M-5-17	185	370	1.00×10^7	run-out	-
M-5-18	190	380	1.00×10^7	run-out	-
M-5-19	192.5	385	1.00×10^7	run-out	-
M-5-20	205	410	251,325	fracture	Mg_2Si
M-5-21	202.5	405	112,467	fracture	Mg_2Si
M-5-22	200	400	228,618	fracture	Mg_2Si
M-5-23	195	390	285,575	fracture	Mg_2Si
M-5-24	197.5	395	209,999	fracture	Mg_2Si
M-5-25	192.5	385	3,296,722	fracture	$Al_{23}CuFe_4+Mg_2Si$

Table A2. Fatigue results of 7050 aluminum alloy FSW joints.

Specimen	σ_a (MPa)	σ_{max} (MPa)	Fatigue Life (Cycles)	Result	Fracture Position	Fracture Phase
J-1-1	165	290	80,671	fracture	−17	$Al_{23}CuFe_4$
J-1-2	216	240	1,791,005	fracture	−13	$Al_{23}CuFe_4$
J-1-3	207	230	1.00×10^7	run-out	-	-
J-1-4	225	250	140,232	fracture	−27	Al-Fe-Cu-Si
J-1-5	225	250	274,147	fracture	−14	Al-Zn-Mg+Mg_2Si
J-1-6	220.5	245	122,771	fracture	−27	Al_7Cu_2Fe
J-1-7	216	240	295,384	fracture	−11	Mg_2Si
J-1-8	216	240	163,309	fracture	14	Mg_2Si
J-1-9	211.5	235	245,078	fracture	13	$Al_{23}CuFe_4$
J-1-10	202.5	225	943,366	fracture	−11.5	Mg_2Si
J-1-11	198	220	902,891	fracture	27	Mg_2Si
J-1-12	198	220	2,219,198	fracture	23	Al-Fe-Cu-Si
J-1-13	198	220	396,098	fracture	5	$Al_{23}CuFe_4+Mg_2Si$
J-1-14	184.5	205	1.00×10^7	run-out	-	-
J-1-15	193.5	215	811,127	fracture	−23	$Al_{23}CuFe_4$
J-1-16	207	230	410,635	fracture	−7	Al-Fe-Cu-Si
J-1-17	207	230	990,881	fracture	−11	Al-Fe-Si
J-1-18	211.5	235	396,522	fracture	−25	Mg_2Si
J-1-19	198	220	2,100,583	fracture	25	Al-Zn-Mg-Cr
J-3-1	196	280	334,717	fracture	−14	Al-Zn-Mg
J-3-2	192.5	275	199,185	fracture	−10	Al-Zn-Mg
J-3-3	185.5	265	1,066,377	fracture	−12	Al_7Cu_2Fe
J-3-4	178.5	255	1.00×10^7	run-out	-	-
J-3-5	182	260	2,710,786	fracture	−10	$Al_{23}CuFe_4$
J-3-6	179.9	257	1.00×10^7	run-out	-	-
J-3-7	183.4	262	1.00×10^7	run-out	-	-
J-3-8	185.5	265	1,100,065	fracture	−12	Mg_2Si
J-3-9	182	260	875,146	fracture	−13	Al-Fe-Si
J-3-10	175	250	7,592,429	fracture	−13	Mg_2Si
J-3-11	175	250	5,932,497	fracture	−12	$Al_{23}CuFe_4$
J-3-12	171.5	245	1.00×10^7	run-out	-	-
J-3-13	189	270	831,811	fracture	15	Al_7Cu_2Fe
J-3-14	183.4	262	706,717	fracture	−13	$Al_{23}CuFe_4$
J-3-15	182	260	256,803	fracture	−27	$Al_{23}CuFe_4$
J-3-16	182	260	1.00×10^7	run-out	-	-
J-3-17	189	270	265,966	fracture	−12	Mg_2Si
J-3-18	185.5	265	4,698,011	fracture	−11	Mg_2Si
J-3-19	185.5	270	1,886,146	fracture	−14	Al-Fe-Cu-Si

Table A2. *Cont.*

Specimen	σ_a (MPa)	σ_{max} (MPa)	Fatigue Life (Cycles)	Result	Fracture Position	Fracture Phase
J-3-20	189	270	292,650	fracture	10	Al-Fe-Cu-Si
J-3-21	189	270	222,860	fracture	15	Mg_2Si
J-3-22	189	270	206,630	fracture	−13	
J-3-23	189	270	247,085	fracture	−27	$Al_{23}CuFe_4$
J-5-1	165	330	205,727	fracture	−12	Al-Zn-Mg-Cr
J-5-2	160	320	165,198	fracture	−12	$Al_{23}CuFe_4$
J-5-3	145	290	1.00×10^7	run-out	-	-
J-5-4	150	300	1.00×10^7	run-out	-	-
J-5-5	157.5	315	680,000	fracture	−11	Al-Zn-Mg
J-5-6	155	310	1.00×10^7	run-out	-	-
J-5-7	157.5	315	293,075	fracture	−12	Mg_2Si
J-5-8	152.5	305	696,085	fracture	−12	$Al_{23}CuFe_4$
J-5-9	150	300	487,210	fracture	−14	Al-Zn-Mg-Cr
J-5-10	145	290	308,020	fracture	−12	$Al_{23}CuFe_4$
J-5-11	135	270	1.00×10^7	run-out	-	-
J-5-12	140	280	1,110,861	fracture	11	Al-Fe-Cu-Si
J-5-13	140	280	1,448,751	fracture	−10	Al-Fe-Cu-Si
J-5-14	138.5	277	1.00×10^7	run-out	-	-
J-5-15	150	300	468,549	fracture	12	Al-Fe-Cu-Si
J-5-16	155	310	632,045	fracture	−18	Al_7Cu_2Fe
J-5-17	152.5	305	404,556	fracture	14	Al-Fe-Cu-Si
J-5-18	152.5	305	377,823	fracture	14	Al-Fe-Cu-Si
J-5-19	150	300	287,060	fracture	−13	$Al_{23}CuFe_4$
J-5-20	155	310	178,972	fracture	14	Al-Zn-Mg
J-5-21	155	310	233,045	fracture	−9.5	Al-Fe-Cu-Si

Appendix B

(**a**) (**b**)

Figure A1. (**a**) Secondary phase of base-material cracking and (**b**) FSW joint cracking phase.

References

1. Çam, G.; Ipekoğlu, G. Recent developments in joining of aluminum alloys. *Int. J. Adv. Manuf. Technol.* **2017**, *91*, 1851–1866. [CrossRef]
2. Threadgill, P.L.; Leonard, A.J.; Shercliff, H.R.; Withers, P.J. Friction stir welding of aluminium alloys. *Int. Mater. Rev.* **2009**, *54*, 49–93. [CrossRef]
3. Dursun, T.; Soutis, C. Recent developments in advanced aircraft aluminium alloys. *Mater. Des.* **2014**, *56*, 862–871. [CrossRef]
4. Wang, D.; Feng, J.; Guo, D.; Sun, C.; Luan, G.; Guo, H. Process of friction-stir welding high-strength aluminum alloy and mechanical properties of joint. *China Weld* **2004**, *13*, 159–162.
5. Ma, Z.Y.; Feng, A.H.; Chen, D.L.; Shen, J. Recent Advances in Friction Stir Welding/Processing of Aluminum Alloys: Microstructural Evolution and Mechanical Properties. *Crit. Rev. Solid State Mater. Sci.* **2018**, *43*, 269–333. [CrossRef]
6. Sun, G.; Wang, C.; Wei, X.; Shang, D.; Chen, S. Study on small fatigue crack initiation and growth for friction stir welded joints. *Mater. Sci. Eng. A* **2019**, *739*, 71–85. [CrossRef]
7. Zheng, Z.Q.; Chen, Y.Y.; Zhong, L.P. Initiation and propagation behavior of fatigue crack in 2524-T34 alloy. *Chin. J. Nonferrous Met.* **2010**, *1*, 43–48.
8. Payne, J.; Welsh, G.; Christ, R.J., Jr.; Nardiello, J.; Papazian, J.M. Observations of fatigue crack initiation in 7075-T651. *Int. J. Fatigue* **2010**, *32*, 247–255. [CrossRef]
9. Harlow, D.; Nardiello, J.; Payne, J. The effect of constituent particles in aluminum alloys on fatigue damage evolution: Statistical observations. *Int. J. Fatigue* **2010**, *32*, 505–511. [CrossRef]
10. Singh, S.S.; Schwartzstein, C.; Williams, J.J.; Xiao, X.; De Carlo, F.; Chawla, N. 3D microstructural characterization and mechanical properties of constituent particles in Al 7075 alloys using X-ray synchrotron tomography and nanoindentation. *J. Alloys Compd.* **2014**, *602*, 163–174. [CrossRef]
11. Jin, Y.; Cai, P.; Wen, W.; Nagaumi, H.; Xu, B.; Zhang, Y.; Zhai, T. The anisotropy of fatigue crack nucleation in an AA7075 T651 Al alloy plate. *Mater. Sci. Eng. A* **2015**, *622*, 7–15. [CrossRef]
12. Deng, C.; Han, Q.; Gong, B.; Gao, R. Effects of the heterogeneous microstructure of a 7050-T7451 aluminum alloy FSW joint on fatigue behavior under different stress ratios. *Mater. Res. Express A* **2019**, *6*, 126583. [CrossRef]
13. Ma, M.; Wang, B.; Liu, H.; Yi, D.; Shen, F.; Zhai, T. Investigation of fatigue crack propagation behavior of 5083 aluminum alloy under various stress ratios: Role of grain boundary and Schmid factor. *Mater. Sci. Eng. A* **2020**, *773*, 138871. [CrossRef]
14. Wang, S.; Liu, J.; Lu, Z.; Chen, D. Cyclic deformation of dissimilar welded joints between Ti–6Al–4V and Ti17 alloys: Effect of strain ratio. *Mater. Sci. Eng. A* **2014**, *598*, 122–134. [CrossRef]
15. Jata, K.V.; Sankaran, K.K.; Ruschau, J.J. Friction-stir welding effects on microstructure and fatigue of aluminum alloy 7050-T7451. *Met. Mater. Trans. A* **2000**, *31*, 2181–2192. [CrossRef]
16. Besel, M.; Besel, Y.; Mercado, U.A.; Kakiuchi, T.; Uematsu, Y. Fatigue behavior of friction stir welded Al–Mg–Sc alloy. *Int. J. Fatigue* **2015**, *77*, 1–11. [CrossRef]
17. Sillapasa, K.; Surapunt, S.; Miyashita, Y.; Mutoh, Y.; Seo, N. Tensile and fatigue behavior of SZ, HAZ and BM in friction stir welded joint of rolled 6N01 aluminum alloy plate. *Int. J. Fatigue* **2014**, *63*, 162–170. [CrossRef]
18. White, B.; White, R.; Jordon, J.; Allison, P.; Rushing, T.; Garcia, L. The effect of tensile pre-straining on fatigue crack initiation mechanisms and mechanical behavior of AA7050 friction stir welds. *Mater. Sci. Eng. A* **2018**, *736*, 228–238. [CrossRef]
19. Hassan, K.A.; Prangnell, P.B.; Norman, A.F.; Price, D.A.; Williams, S.W. Effect of welding parameters on nugget zone microstructure and properties in high strength aluminum alloy friction stir welds. *Sci. Technol. Weld. Join.* **2003**, *8*, 257–268. [CrossRef]
20. Moshtaghi, M.; Loder, B.; Safyari, M.; Willidal, T.; Hojo, T.; Mori, G. Hydrogen trapping and desorption affected by ferrite grain boundary types in shielded metal and flux-cored arc weldments with Ni addition. *Int. J. Hydrogen Energy* **2022**, *47*, 20676–20683. [CrossRef]
21. Laz, P.J.; Hillberry, B.M. Fatigue life prediction from inclusion initiated cracks. *Int. J. Fatigue* **1998**, *20*, 263–270. [CrossRef]
22. Frommeyer, G.; Beer, S.; Oldenburg, K.V. Microstructure and Mechanical Properties of Mechanically Alloyed Intermetallic Mg2Si Al Alloys. *Z. Met.* **1994**, *85*, 372–377.
23. Liu, Y.; Deng, C.; Gong, B.; Bai, Y. Effects of heterogeneity and coarse secondary phases on mechanical properties of 7050-T7451 aluminum alloy friction stir welding joint. *Mater. Sci. Eng. A* **2019**, *764*, 138223. [CrossRef]